Role of phosphate concentration in control for phosphate removal and recovery by layered double hydroxides

Yin Xu[1] · Tingjiao Liu[1] · Yukun Huang[1] · Jiayi Zhu[1] · Runliang Zhu[1]

Abstract

Phosphorus removal from wastewater has become urgent because of eutrophication control. Phosphate concentration in control for phosphate removal and recovery by Mg–Fe oxide has been investigated. The results show that the adsorption capacity of phosphate by Mg–Fe oxide calcined at 450 °C was 28.3 mg/g, and it was kept at wide optimal adsorption pH ranges (4–10). The coexisting ions had influenced phosphate adsorption process and the order is $CO_3^{2-} > SO_4^{2-} > NO_3^- > Cl^-$, with the inhibition rate of CO_3^{2-} being 43%. Interestingly, phosphate concentration plays an important role in phosphate removal by Mg–Fe oxide. Under higher initial phosphate concentrations (200–800 mg/L), Sips model was well fitted. In addition, the adsorption kinetics was well described by the pseudo-second-order kinetic model before 25 min and the pseudo-first-order kinetic model after 25 min. In contrast, Langmuir model and pseudo-second-order kinetic model were fitted under lower initial phosphate concentrations (20–200 mg/L). The results of XRD, XPS, SEM, and TEM characterization show that $Mg_3(PO_4)_2$ was formed by surface precipitation under 800 mg/L phosphate solution, and Mg–Fe layered structure was present via the unique memory effect under 20 mg/L phosphate solution. Mg–Fe oxide can be recovered through CO_3^{2-} ion exchange, and the removal efficiency of phosphate was 56% after seven cycles.

Keywords Mg–Fe oxide · Phosphate · Adsorption mechanism

Introduction

Phosphorus is an essential nutrient and tends to be the most limiting factor for all life growth on this planet (Hu et al. 2018; Li et al. 2016b, 2018; Ooi et al. 2017). Any source of excess phosphate ions entering a water body has the potential to trigger eutrophication which has impacts on recreation, ecology, esthetics, and drinking water treatment (Ajmal et al. 2018; Fu et al. 2018; Lin et al. 2019a). If people drink high phosphate water, it will lead to the calcium in the body not being fully absorbed and utilized, which is easy to cause fracture, tooth loss, and bone deformation (Saberzadeh et al. 2016; Zhong et al. 2015). New regulations call for significant reduction in phosphorus concentration in China, so it needs to find new technology or novel materials for phosphorus removal (Cai et al. 2012; Li et al. 2019; Zhan et al. 2016). Biological treatment technique has been wildly applied for phosphorus removal in wastewater treatment. However, the temperature, pH, and organic loading of the wastewater have great influence on the phosphorus removal efficiency; thus, its effluent has difficulty in meeting emission standard (Bouraiea and Masoud 2017; Lin et al. 2019b; Zhang et al. 2018). Adsorption as advanced treatment technique is adopted to treat phosphorus wastewater because of high removal efficiency (Boeykens et al. 2017; Kong et al. 2019; Ogata et al. 2016; Rashid et al. 2017). At the same time, adsorption is a very effective separation technology, which has the characteristics of low cost, simple design, easy operation, and environmental friendliness (Foroutan et al. 2019c, d; Shams et al. 2013; Shafiee et al. 2019).

Layered double hydroxides (LDHs) have attracted increased attention as sorbents in the removal of aqueous pollutants, such as phosphorous, dyes, and bromate (Guo et al. 2019; Yan et al. 2015; Zhang et al. 2013). Large surface and high anion exchange capacity make LDHs promising

---

✉ Yin Xu
  xuyin@xtu.edu.cn

[1] Department of Environment, College of Environment and Resources, Xiangtan University, Xiangtan 411105, Hunan, People's Republic of China

materials for phosphorus adsorption from wastewater. An increase of the sorption capacity of LDHs is conducive by their calcination at 300–500 °C, which results in the formation of a uniform mixture of double oxides. Calcined LDH products (CLDHs) in contact with aqueous solution are characterized by manifestation of the memory effect; thus, anions can be easily adsorbed to the interlayer spacing and the external surface. Also CLDHs release metal cations and their hydroxides in aqueous solution to buffer pH; high adsorption capacity was maintained in ranges of pH 4–10 (Hatami et al. 2018; Iftekhar et al. 2018). In general, multiple mechanisms including surface adsorption, surface precipitation, and anion exchange in the interlayer contribute to the removal of phosphorus by the LDH-type materials (Li et al. 2016a; Novillo et al. 2014). The predominant adsorption mechanisms are related to the temperature of heat treatment, metal content, anion concentration, and so on (Jia et al. 2016; Seftel et al. 2018). To date, there are still many open questions and challenges requiring further investigations in role of phosphate ions concentration in control for phosphate removal and recovery by CLDHs (Ding et al. 2017; Yan et al. 2015). Therefore, it is hypothesized that understanding the CLDH structure in different concentration of phosphate ions aqueous solution is crucial for realizing high-performance phosphate recovery and the modification of materials.

The objective of this study was to determine role of phosphate ion concentration in control for phosphate ion removal and recovery by Mg–Fe hydroxide and Mg–Fe oxide. The reason for choosing magnesium and iron is that they are less toxic, environmentally friendly, and cheap (Mortazavi et al. 2011; Ramavandi et al. 2011, 2013). The phosphate ion adsorption mechanism by Mg–Fe oxide under different phosphate ion concentrations was explained by the adsorption isotherm, kinetics, morphology, crystal structure, and valence state.

Materials and methods

Materials

The chemical used for this project, including $Mg(NO_3)_2 \cdot 6H_2O$ (99.0%), $Fe(NO_3)_3 \cdot 9H_2O$ (98.5%), Na_2CO_3 (99.8%), NaOH (96.0%), HCl (96.0%), and KH_2PO_4 (99.5%), were purchased from Fengchuan Chemical Co. Ltd. All the chemical solutions were prepared with the deionized water throughout the experiment.

Preparation of Mg–Fe hydroxide and Mg–Fe oxide

Mg–Fe hydroxide was synthesized by coprecipitation method with $Mg(NO_3)_2 \cdot 7H_2O$ and $Fe(NO_3)_3 \cdot 9H_2O$ (Mg/Fe molar ratio 4:1) at pH 10 ± 0.2 (Wan et al. 2017). Mg–Fe oxide was

obtained by the calcination process of the as-prepared Mg–Fe hydroxide under different temperatures (200 °C, 300 °C, 450 °C, 500 °C, 600 °C) for 3 h in a tube furnace.

Characterization of the samples

X-ray diffraction (XRD) patterns of the as-prepared samples were recorded on a Philips Panalytical X'Pert PROX-ray diffractometer (PANalytical, Almelo, The Netherlands), using Cu Kα radiation, to determine the stacking structures of the respective samples at a scan rate of $0.022 \, \theta/s^{-1}$ in the 2θ range of 5°–90°. The applied current and accelerating voltage were 30 mA and 40 kV, respectively.

The thermal stability of the samples was studied by thermogravimetric analysis (TGA, STA449-F5, NETZSCH, Germany) in N_2 atmosphere from 30 to 1000 °C with a ramp rate of 10 °C/min.

X-ray photoelectron spectroscopy (XPS) patterns of the samples were recorded on a Thermo Fisher Scientific ESCALAB250 X-ray spectrometer (Waltham, MA, USA), fitted with a monochromatic Al excitation source (1486.6 eV, 15 kV, 10 mA). All spectra were calibrated to the C 1 s peak (binding energy at 284.6 eV) for the adventitious carbon.

The morphology and particle size of the sample were characterized by transmission electron microscopy (JEM-2100, JEOL, Tokyo, Japan), operated with an accelerating voltage of 200 kV, and magnification ranges of 0.5–1.5 million times. All the sample specimens for TEM studies were ultrasonically dispersed in ethanol, and one or two drops of the upper solution were pipetted out on a micro-mesh cupper grid. Before the TEM analysis, the sample specimens were vacuum-dried in the microscope column for 7–8 min.

Adsorption experiments

All the batch adsorption experiments were performed in stirred on a shaker equipped with a thermostat at 200 rpm and 25 ± 2 °C. The 100 mg/L phosphate ion solutions were prepared by dissolving KH_2PO_4 in deionized water. The pH of the phosphate ion solution was adjusted to a certain value by using 1.0 mol/L NaOH and HCl solutions. After adsorption, the suspension was immediately filtered with a 0.22-μm microfiltration membrane. The adsorption capacity (q_e, mg/g) of the sorbent material for phosphate ions was calculated by the mass balance as expressed in Eq. (1).

$$q_e = \frac{V(C_i - C_e)}{m} \tag{1}$$

where C_i and C_e are the initial and equilibrium concentration of phosphate ions in solution after adsorption process (mg/L) respectively, V is the volume of solution (L), and m is the sorbent mass (g).
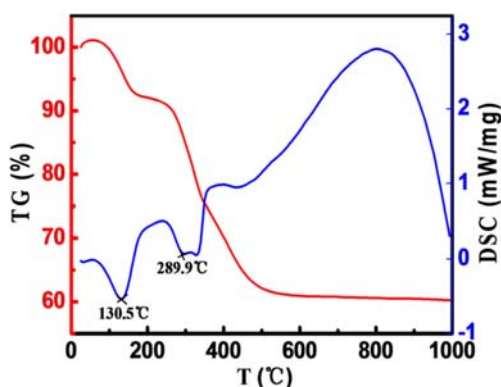
Fig. 1 TG-DSC curves of the Mg–Fe hydroxide

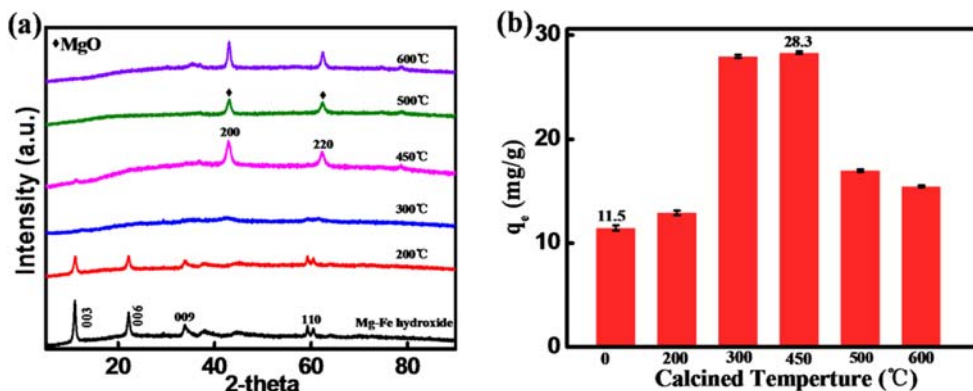**Table 1** BET area of MgFe-LDH calcined at different temperatures

Material	BET area (m^2/g)	Pore volume (cm^3/g)
MgFe-LDH	52.1	0.3603
MgFe-200	65.2	0.3875
MgFe-300	85.6	0.4445
MgFe-450	84.8	0.4191
MgFe-500	75.9	0.3704
MgFe-600	66.2	0.1877

Kinetic adsorption of phosphate ions

Adsorption kinetics of phosphate ions was carried out by mixing a series of 2.0 g adsorbent with 600 ml phosphate ions solution (20, 100, 800 mg/L) in a conical flask. The mixtures were then constant temperature oscillation at 200 rpm at 25 ± 0.2 °C. Two-milliliter solution sample was obtained at a series of designated times for the measurement of phosphate ion concentrations. The concentration of phosphate ions in the filtrates was analyzed. Pseudo-first-order and pseudo-second-order kinetic models were used to fit the adsorption experiment date (Martin et al. 2018).

Adsorption isotherm of phosphate ions

Phosphate ion adsorption isotherms were determined by mixing 0.1-g sample with 30 mL of a series of P solutions (pH 5.0, 20–800 mg/L phosphate ions) in a polyethylene centrifuge tube. After overnight mixing, samples were filtrated through a 0.22-μm microfiltration membrane. The concentration of phosphate ions in the filtered was analyzed. Langmuir, Freundlich, and Sips isotherm models were used for phosphate ion adsorption isotherms (Jang and Lee 2019; Najib and Christodoulatos 2019).

Langmuir, Freundlich, and Sips equations were used to fit the adsorption isotherm data.

Langmuir equations : $q_e = k_L Q C_e / (1 + k_L C_e)$

Freundlich equations : $q_e = k_f C^{1/n}$

Sips equations : $q_e = k Q C_e^{1/n} / \left(1 + k C_e^{1/n}\right)$

where Q is the maximum adsorption capacity; q_e is the adsorption capacity at equilibrium; C_e is the concentration at equilibrium; k_L, k_f, and k are the constants of Langmuir, Freundlich, and Sips equations respectively; n is the non-mean system.

The recovery of Mg–Fe oxide and regeneration experiments

Mg–Fe oxide adsorbed in 20 mg/L phosphate solution was used for desorption, regeneration, and recycling. The Mg–Fe oxide adsorbing 20 mg/L phosphate ion solution was washed by 10% Na_2CO_3 (stripping agent) for 12 h. The mixture was filtered, was dried, and then obtained regenerated Mg–Fe oxide by calcinations at 450 °C for 3 h in a tube furnace. The regenerated Mg–Fe oxide again adsorbed 20 mg/L phosphate ion solutions. Then the adsorption–desorption processes were repeated for seven consecutive cycles.

Fig. 2 Powder XRD patterns (**a**) and the phosphate ions adsorption capacity (**b**) of the Mg–Fe hydroxide
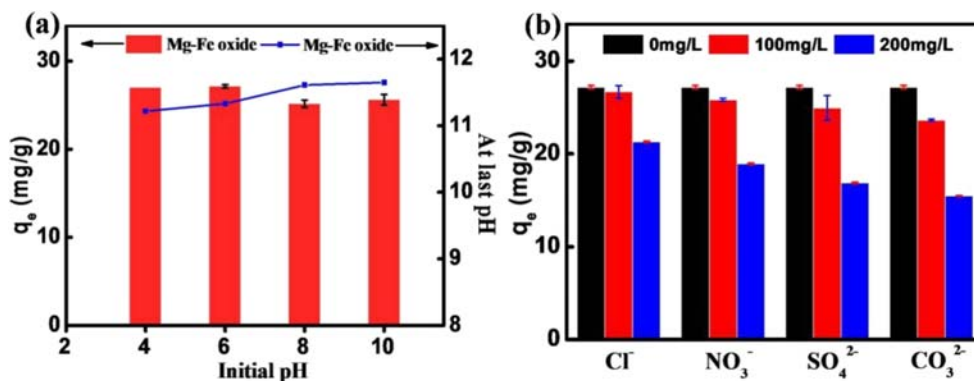
Results and discussion

TG-DSC curves of Mg–Fe hydroxide

The Mg–Fe hydroxide was decomposed in the calcination process, revealing the transformation of Mg–Fe hydroxide into Mg–Fe oxides. TG-DSC curves of Mg–Fe hydroxide is shown in Fig. 1. In the DSC curve, two endothermic peaks were detected correspondingly in this temperature range. The first peak at 130.5 °C is present corresponding to the loss of physically adsorbed water molecules. Then, the peak at 289.9 °C is associated with the removal of H_2O and anion in the interlayer. As the temperature increased to 450 °C, the anion is completely removed and the total weight loss of the catalyst reached 39.0% in the TG curve (Foroutan et al. 2018a, b, c). The weight in the three steps became constant when the temperature exceeded 450 °C.

Powder XRD pattern and phosphate ion adsorption capacity of the Mg–Fe hydroxide under different calcination temperatures

The powder XRD patterns of the Mg–Fe hydroxide under different calcination temperatures are shown in Fig. 2a. The characteristic reflection peaks for (003), (006), (009), and (110) planes were present when the calcination temperature

was under 200 °C, owing to the well-crystallized layered structure of hydrotalcite-like type material (Bai et al. 2017). The characteristic peak intensity of hydroxide became extremely weak and the characteristic peak intensity of oxide began to appear at 300 °C. The diffraction intensity of LDH becomes weak with the increase of the temperature, as a result of the interlaminar collapse. The characteristic reflection peaks for layer structure completely disappeared and all diffraction peaks were corresponding well to the MgO when the calcination temperature was more than 450 °C. The adsorption capacity initially increased with increasing temperature and decreased after 450 °C. Table 1 present the BET area of MgFe-LDH calcined at different temperatures, similar with the tread of its adsorption capacity, indicating that surface area was important in the adsorption process (Wang et al. 2016a, b; Lai et al. 2016; Sadeghalvad et al. 2017). The adsorption capacity of phosphate by Mg–Fe oxide calcined at 450 °C was 28.3 mg/g. There was no the characteristic diffraction peaks of iron oxide in the XRD results of the Mg–Fe oxide.

The phosphate ion adsorption by Mg–Fe hydroxide under different calcination temperatures is illustrated in Fig. 2b. The max adsorption phosphate ion capacity was 28.3 mg/g by the Mg–Fe oxide with the treatment of calcination at 450 °C, which was 2.46-fold higher than that of the Mg–Fe hydroxide without calcination.
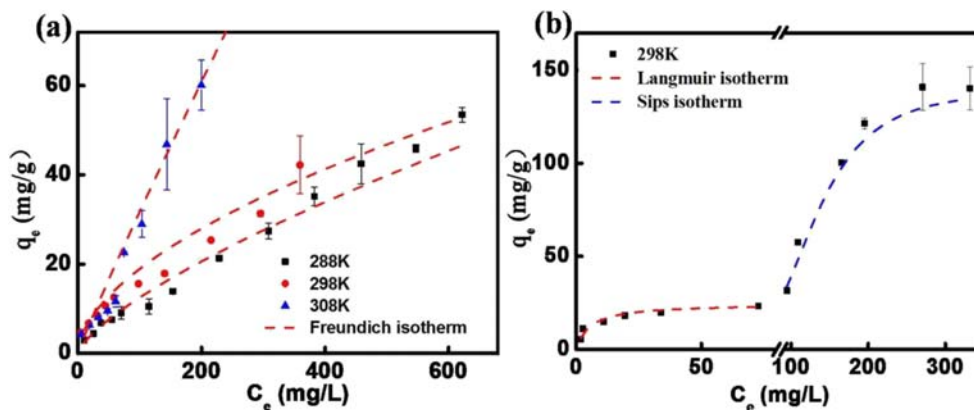
Table 2 Standard thermodynamic constant (ΔG^0, ΔS^0, ΔH^0) with phosphate adsorption on MgFe-LDH

	温度(K)	ΔG^0 (KJ·mol^{-1})	ΔS^0 (KJ·mol^{-1}·K^{-1})	ΔH^0 (KJ·mol^{-1})
MgFe-LDH	288	− 10.679		
	298	− 11.807	0.204	48.06
	308	− 14.759		

Influence of pH value and competitive ion on phosphate ions adsorption by the Mg–Fe oxide

The pH is one of the important parameters to control the surface charge of the adsorbent and species of adsorbate in an aqueous medium (Esvandi et al. 2018; Foroutan et al. 2019b). As shown in Fig. 3a, the capacity of phosphate ion adsorption at solutions with different initial pH range (4–10) was negligible change proving that Mg–Fe oxide kept strong adsorption performance at wide optimal adsorption pH ranges. In addition, the last pH value after adsorption experiments was maintained at 11–12 owing to the buffering capacity of ·OH groups on the surface of Mg–Fe oxide. With the elevation of pH, the amount of positive charge in the aqueous solution declines, and thus the competition between pollutants and positive ions to occupy the adsorbent surface diminishes (Foroutan et al. 2019b).

Municipal and industrial waters always contain coexistent anions, including Cl$^-$, NO$_3^-$, SO$_4^{2-}$, and CO$_3^{2-}$, which may compete with phosphate ions for the binding sites. The influence of competitive anions on phosphate ion adsorption varies based on different adsorbent species. As shown in Fig. 3b, the influence order on the adsorption capacity of phosphate ions is CO$_3^{2-}$ > SO$_4^{2-}$ > NO$_3^-$ > Cl$^-$. In the presence of 200 mg/L CO$_3^{2-}$, the adsorption capacity of phosphate ions was lower than that without CO$_3^{2-}$, the inhibition efficiency was 43.0%. This fact indicates that CO$_3^{2-}$ has stronger combination ability with Mg–Fe oxide than other anions.

Fig. 5 Adsorption kinetics of the Mg–Fe hydroxide (**a**) and the Mg–Fe oxide (**b**, **c**) under different initial phosphate ion concentrations (20 mg/L, 100 mg/L, 800 mg/L)
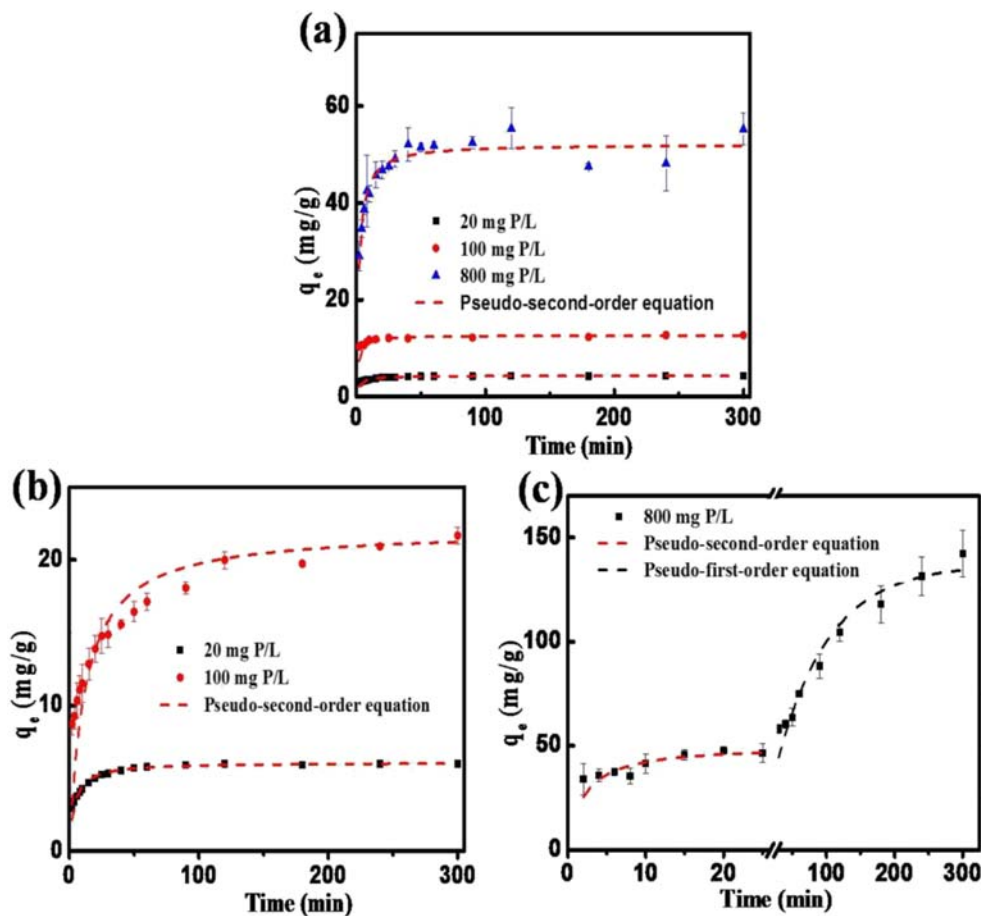
Table 3 Phosphorus removal capacity of different adsorbents

Material	pH	q_e (mg P/g)	Reference
$Fe_3O_4@ZrO_2$	NA	27.93–69.44	(Wang et al. 2016b)
Fe-Si-La	NA	27.80	(Lai et al. 2016)
Ni-Fe HPI	NA	29.89	(Sadeghalvad et al. 2017)
Ceramic	4–10	5.96	(Wang et al. 2016a)

Adsorption isotherms of phosphate ions by Mg–Fe hydroxide and Mg–Fe oxide

Adsorption isotherms describe the relationship between the equilibrium adsorbate concentration in the solution and the amount of phosphate ions adsorbed on the adsorbent. Adsorption isotherms of phosphate ions by the Mg–Fe hydroxide and the Mg–Fe oxide are shown in Fig. 4. The phosphate ion adsorption amount was increased dramatically and then reached equilibrium gradually with the increase of initial phosphate ion concentration from Fig. 4a. Freundlich model ($R^2 = 0.98$, $n = 1.78$, $k_f = 1.425$) was fitted and calculated q_m close to the value determined by the experiment, assuming multilayer coverage on the Mg–Fe hydroxide surface with identical adsorption sites (Ashekuzzaman and Jiang 2017; Xi et al. 2019). In addition, the equilibrium uptake capacity of phosphate ions was increased with the rise of temperature. Table 2 presents standard thermodynamic constant (ΔG^0, ΔS^0, ΔH^0) with phosphate adsorption on MgFe-LDH. The adsorption process of phosphate ions by the Mg–Fe hydroxide was endothermic reaction because of $\Delta G^0 \leq 0$ (Halajnia et al. 2013). Interestingly, adsorption isotherm of phosphate ions by Mg–Fe oxide was divided into two stages: Langmuir model was fitted under lower initial phosphate ions concentrations (20–200 mg/L), suggesting that the adsorption sites on the Mg–Fe oxide of surface were homogeneous and the adsorption was monolayer adsorption (Fig. 4b) (Bonyadi et al. 2019; Foroutan et al. 2020). Under higher initial phosphate ion concentrations (200–800 mg/L), the Sips model was better fitted (Foroutan et al. 2019a). The Sips isotherm model is a versatile

isotherm expression that can simulate both Langmuir and Freundlich behaviors (Vikrant et al. 2018; Yang et al. 2019). The adsorption process was attributed to multiple adsorbent–adsorbate interactions such as hydrogen bonding, π–π stacking, and pore filling (Okoli et al. 2014). Thus, different phosphate ion concentrations have different adsorption mechanisms by Mg–Fe oxide.

Kinetic adsorption under different phosphate ion concentrations

Kinetic adsorption is one of the most important factors in evaluating the efficiency of an adsorbent (Esvandi et al. 2018; Foroutan et al. 2019c). Kinetic adsorption of phosphate ions by Mg–Fe hydroxide and Mg–Fe oxide under different phosphate ion concentrations is shown in Fig. 5. The adsorption of phosphate ions by Mg–Fe hydroxide has reached equilibrium quickly at 40 min under 20 mg/L, 100 mg/L, and 800 mg/L phosphate ion concentrations (Fig. 5a). All kinetic data for Mg–Fe hydroxide under different phosphate ion concentrations could be well described by the pseudo-second-order kinetic model, indicating that the chemisorption involving sharing or exchange of electrons dominates the whole adsorption process (Yang et al. 2014). Similarly, the kinetic adsorption of phosphate ions by Mg–Fe oxide was well described by the pseudo-second-order kinetic model under 20 mg/L and 100 mg/L phosphate ion concentrations (Fig. 5b). Differently, the kinetic adsorption under 800 mg/L phosphate ion concentration was well described by the pseudo-second-order kinetic model before 25 min and the pseudo-first-order kinetic model after 25 min (Fig. 5c). The phosphate ion adsorption capacity strongly depended on the initial phosphate ion concentration of solution. Table 3 presents phosphorus removal capacity of different adsorbents. Under higher phosphate ion concentration, the adsorption capacity of phosphate ions by Mg–Fe oxide was larger than that by other adsorbents.

Fig. 6 Powder XRD patterns of the Mg–Fe hydroxide (a) and Mg–Fe oxide (b) after phosphate uptake
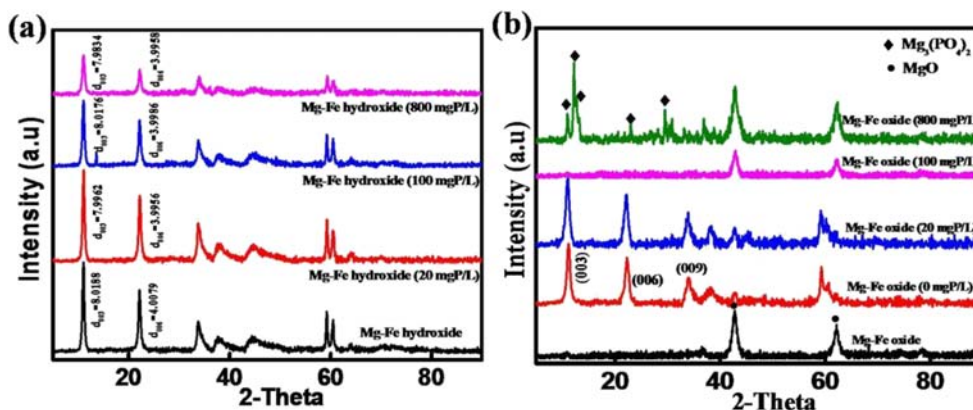
Fig. 7 XPS spectra of the Mg–Fe hydroxide (**a**) and Mg–Fe oxide (**b**) of before adsorption phosphate ion and after phosphate ion uptake
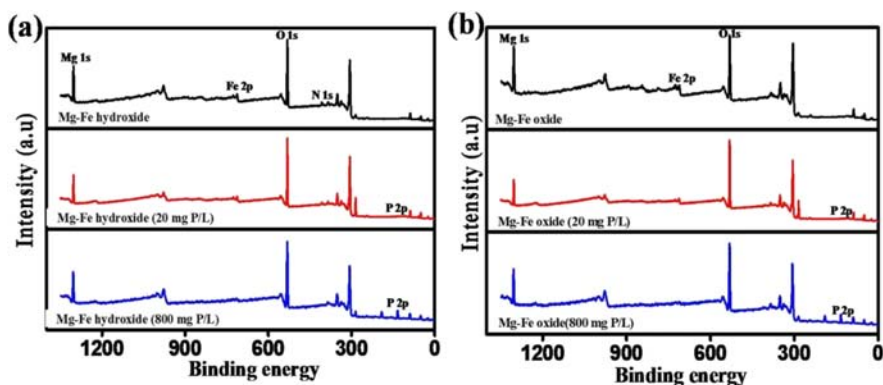

Fig. 8 O 1 s XPS spectra of the Mg–Fe hydroxide and Mg–Fe oxide after phosphate ion uptake at different initial phosphate ion concentrations (20 mg/L, 800 mg/L)
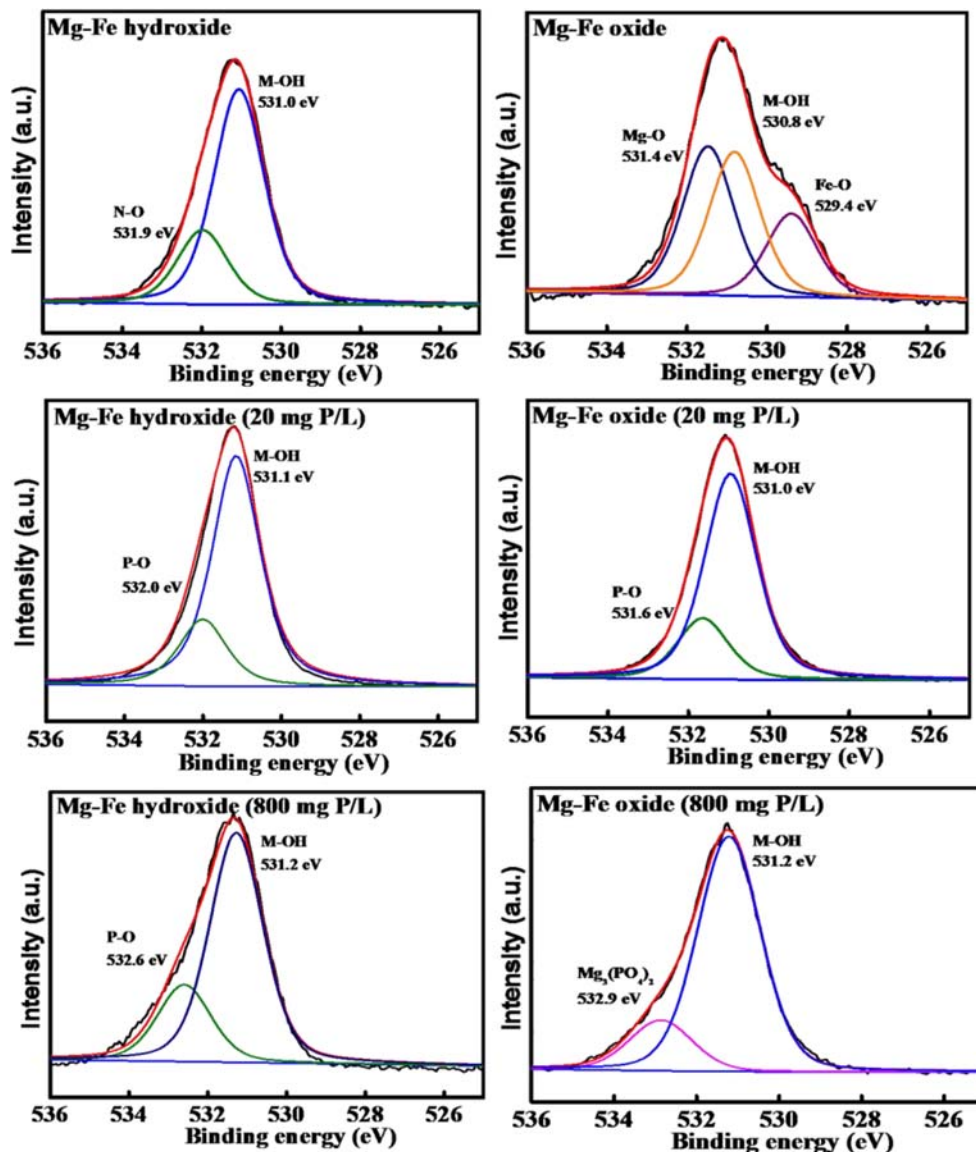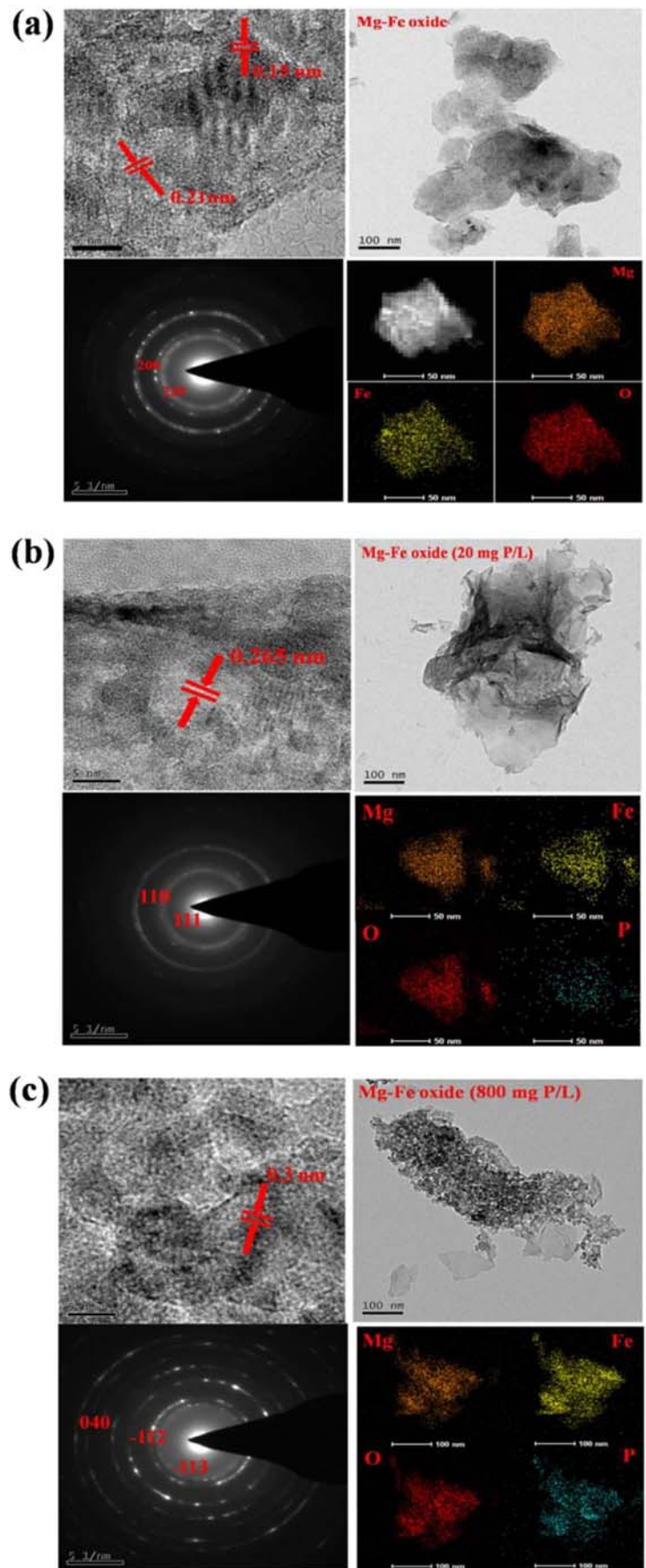
Fig. 9 Typical TEM, HRTEM, the corresponding SAED patterns, and EDS of **a** Mg–Fe oxide, **b** Mg–Fe oxide (20 mg P/L), and **c** Mg–Fe oxide (800 mg P/L)

Adsorption mechanism of phosphate ions by the Mg–Fe hydroxide and the Mg–Fe oxide under different phosphate ion concentrations

The XRD, XPS, SEM, and TEM characterization of Mg–Fe hydroxide and Mg–Fe oxide in the adsorption process was further to study phosphate ion adsorption mechanism. Figure 6 illustrates the powder XRD patterns of the Mg–Fe hydroxide and the Mg–Fe oxide after adsorption under different phosphate ion concentrations. As shown in Fig. 6a, the powder XRD patterns of the Mg–Fe hydroxide have indicated sharp and symmetric reflections assigned to the basal (003), (006), and (009) planes together with the asymmetric, according to highly crystalline hydroxide layer structures. The calculated basal spacing of Mg–Fe hydroxide is ~ 0.802 nm, while the spacing of Mg–Fe hydroxide after absorbing phosphate ions is smaller than the precursor. It is further proved that phosphate ions can be adsorbed through anionic exchange. As shown in Fig. 6b, the sample after absorbing 20 mg/L phosphate ion concentration by Mg–Fe oxide has already appeared characteristic diffraction peaks of Mg–Fe hydroxide (PDF#) because the Mg–Fe oxide can take place the spontaneous rehydration, and LDH structure is recovered in aqueous solutions. After absorbing 100 mg/L phosphate ion concentration of Mg–Fe oxide, the characteristic diffraction peaks of MgO (PDF#) were present. After absorbing 800 mg/L phosphate ion concentration, the characteristic diffraction peaks for $Mg_3(PO_4)_2$ (PDF#) suggest ion precipitation on the surface of Mg–Fe oxide. The predominant adsorption mechanism contributes to reconstruction process at lower phosphate ion concentrations and the surface precipitation at higher concentrations.

Iron was not found in the XRD patterns; XPS spectra of Mg–Fe hydroxide and the Mg–Fe oxide were further investigated. The XPS spectra of the Mg–Fe hydroxide and the Mg–Fe oxide after adsorption under 20 mg/L and 800 mg/L phosphate ion concentrations are shown in Fig. 7. The presence of Mg, Fe, and O was detected in all XPS spectra. After phosphate ion adsorption, the spectrum of phosphate ions (2p) at a binding energy of 132–136 eV was present in the post-adsorption sample.
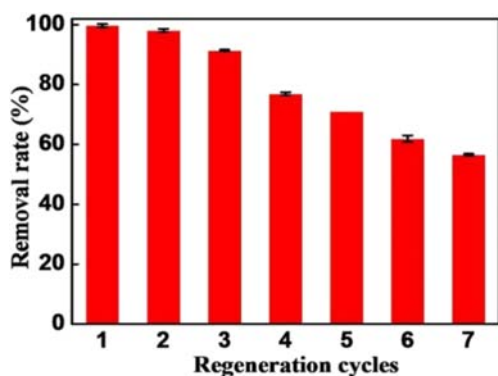
XPS spectra of oxygen element were conducted to investigate the surface chemical state of oxygen before and after adsorption of 20 mg/L and 800 mg/L phosphate ions. As shown in Fig. 8, the O 1 s peaks for the Mg–Fe hydroxide, Mg–Fe hydroxide (20 mg/L), and Mg–Fe hydroxide (800 mg/L) could be well fitted with two overlapped O 1 s peaks, including oxide oxygen (O^{2-}) and metal hydroxyl group (Me–OH). The binding energy of oxide oxygen after the phosphate ion adsorption was shifted to higher energy, indicating that P–O was instead of N–O by anion exchange. Mg–Fe oxide has a more peak corresponding to metal oxide (Me–O). After adsorption, Mg–Fe oxide (20 mg/L) only appeared O^{2-} and –OH of two overlapped O 1 s peaks, similar with Mg–Fe hydroxide, demonstrating reassembled hydrotalcite structure. The binding energy of oxide oxygen after 800 mg/L phosphate ion adsorption was shifted to 532.9 eV corresponding to $Mg_3(PO_4)_2$ peak.

The morphology of the Mg–Fe oxide before and after adsorption characterized by HRTEM is shown in Fig. 9. The Mg–Fe oxide was the collapsed plate-like structure upon the calcination process. After adsorption of 20 mg P/L, Mg–Fe oxide was layer structures because that phosphate ions take part in the reconstruction of the LDH through "memory effect" (Fig. 9b). The surface of Mg–Fe oxide (800 mg P/L) has particle formation (Fig. 9c). Some sets of selected area electron diffraction (SAED) pattern respectively from the Mg–Fe oxide, Mg–Fe oxide (20 mg P/L), and Mg–Fe oxide (800 mg P/L) matrix can be distinguished clearly. The as-observed lattice spacing in the HRTEM image was calculated to be 0.21 nm and 0.15 nm, matching well with the (200) and (220) plane of hexagonal Mg–Fe oxide. It indicated the (200) and (220) facet of mixed metal oxide lattice. Lattice spacing of Mg–Fe oxide (20 mg P/L) in the HRTEM image was calculated to be 0.265 nm, matching well with the (110) and (111) plane of Mg–Fe oxide (20 mg P/L) and consisting with XRD of patterns. Lattice spacing of Mg–Fe oxide (800 mg P/L) in the HRTEM image was calculated to be 0.3 nm, indicating the precipitation of magnesium phosphate ions. The EDS elemental mapping images of Mg, Fe, O, and P of Mg–Fe oxide before and after phosphate ion adsorption were presented. The green dots representing phosphate ion elements distributed uniformly on the entire surface of Mg–Fe oxide as shown in Fig. 9b, determining the fact that the phosphate ions were intercalated into the interlayer galleries of Mg–Fe oxide via reconstruction process for Mg–Fe oxide (20 mg P/L). It was observed the Mg, Fe, and O distribution overlapped well with phosphate ions in the whole sample surface for Mg–Fe oxide (800 mg P/L), which further explain that the magnesium phosphate ions had formed on the surface of Mg–Fe oxide.

Solid adsorbent regeneration

In order to investigate the recycle of Mg–Fe oxide under 20 mg/L phosphate ion solution, desorption through Na_2CO_3 was tested and the removal efficiency of phosphate

Fig. 10 The removal efficiency of phosphate ions by the regenerated Mg–Fe oxide

Fig. 11 The phosphate ion adsorption mechanism by Mg–Fe oxide under different phosphate ion concentrations
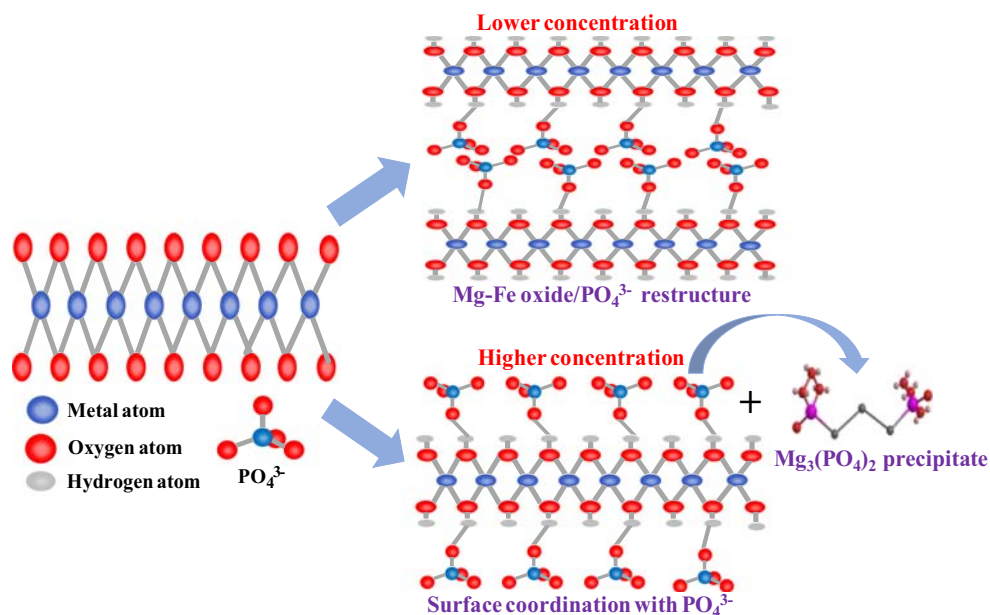
ions by regenerated Mg–Fe oxide is shown in Fig. 10. The reusability of the solid adsorbents is considered a potential economical parameter, investigated by reusing the solid adsorbent that embedded phosphate ions. The removal efficiency of phosphate ions was decreased with the increased of recycle times, which still can maintain above 56% for phosphate ion adsorption after seven times. Therefore, the results indicated the sodium carbonate as the better efficient desorbed for adsorbed phosphate ions on Mg–Fe oxide. It implied that the Mg–Fe oxide shows good stability and reusability for phosphate ion adsorption.

The phosphate ion adsorption mechanism by Mg–Fe oxide under different phosphate ions concentrations is illustrated in Fig. 11. For lower phosphate ion concentration, the reconstruction process assisted the adsorption of phosphate ions onto Mg–Fe oxide (Okoli et al. 2015). With the increase of phosphate ion concentration in the external environment, the phosphate ions directly bind with the surface of Mg–Fe oxide by surface complexation (Okoli et al. 2014; Okoli and Ofomaja 2019). For higher phosphate ion concentration, the precipitation of $Mg_3(PO_4)_2$ was formed. Thus, different concentration phosphate ions could be adsorbed by Mg–Fe oxide with different ways.

Conclusion

In this study, the role of phosphate concentration in control for phosphate removal and recovery by Mg–Fe oxide was investigated. After calcination of Mg–Fe LDHs, Mg–Fe oxide has higher adsorption capacity of phosphate and was kept at wide optimal adsorption pH ranges. The coexisting ions (CO_3^{2-}, SO_4^{2-}, NO_3^-, Cl^-) had influenced phosphate adsorption

process. Combined with the characterization of XRD, XPS, SEM, and TEM, the adsorption isotherm and kinetics on phosphate ion adsorption by Mg–Fe hydroxide indicates that an anion exchange is the main adsorption mechanism in the wide concentration of phosphate ion concentration. However, Mg–Fe oxide has different adsorption mechanisms under different phosphate ion concentrations. The results confirmed anionic exchange at lower phosphate ion concentrations and surface precipitation at higher phosphate ion concentrations in the adsorption process. Efficient desorption of phosphate ions and regeneration of adsorbents using CO_3^{2-} made the developed adsorbents a viable alternative to the common adsorbents available for treatment of aqueous phosphate ion pollution. Finally, the results are the importance of the understanding the interaction between the Mg–Fe oxide and phosphate, which is better to prepare the higher efficiency adsorbent and optimization of the adsorption process.

References

Ajmal Z, Muhmood A, Usman M, Kizito S, Lu J, Dong R, Wu S (2018) Phosphate removal from aqueous solution using iron oxides: adsorption, desorption and regeneration characteristics. J Colloid Interface Sci 528:145–155

Ashekuzzaman SM, Jiang JQ (2017) Strategic phosphate removal/recovery by a re-usable Mg–Fe–Cl layered double hydroxide. Process Saf Environ 107:454–462

Bai JF, Liu Y, Yin XH, Duan HT, Ma JH (2017) Efficient removal of nitrobenzene by Fenton-like process with Co-Fe layered double hydroxide. Appl Surf Sci 416:45–50

Boeykens SP, Piol MN, Samudio LL, Saralegui AB, Vazquez C (2017) Eutrophication decrease: phosphate adsorption processes in presence of nitrates. J Environ Manag 203(Pt 3):888–895

Bonyadi Z, Kumar PS, Foroutan R, Kafaei R, Arfaeinia H, Farjadfard S, Ramavandi B (2019) Ultrasonic-assisted synthesis of Populus alba activated carbon for water defluorination: application for real wastewater. Korean J Chem Eng 36(10):1595–1603

Cai P, Zheng H, Wang C, Ma H, Hu J, Pu Y, Liang P (2012) Competitive adsorption characteristics of fluoride and phosphate on calcined Mg-Al-CO$_3$ layered double hydroxides. J Hazard Mater 213-214:100–108

Ding H, Zhao Y, Duan Q, Wang J, Zhang K, Ding G, Xie X, Ding C (2017) Efficient removal of phosphate from aqueous solution using novel magnetic nanocomposites with Fe$_3$O$_4$ @SiO$_2$ core and mesoporous CeO$_2$ shell. J Rare Earths 35(10):984–994

Bouraiea ME, Masoud AA (2017) Adsorption of phosphate ions from aqueous solution by modified bentonite with magnesium hydroxide Mg(OH)$_2$. Appl Clay Sci 140:157–164

Esvandi Z, Foroutan R, Mirjalili M, Sorial GA, Ramavandi B (2018) Physicochemical behavior of Penaeuse semisulcatuse chitin for Pb and Cd removal from aqueous environment. J Polym Environ 27(2): 263–274

Foroutan R, Ahmadlouydarab M, Ramavandi B, Mohammadi R (2018a) Studying the physicochemical characteristics and metals adsorptive behavior of CMC-g-HAp/Fe$_3$O$_4$ nanobiocomposite. J Environ Chem Eng 6(5):6049–6058

Foroutan R, Mohammadi R, Ramavandi B, Bastanian M (2018b) Removal characteristics of chromium by activated carbon/ CoFe$_2$O$_4$ magnetic composite and Phoenix dactylifera stone carbon. Korean J Chem Eng 35(11):2207–2219

Foroutan R, Zareipour R, Mohammadi R (2018c) Fast adsorption of chromium (VI) ions from synthetic sewage using bentonite and bentonite/bio-coal composite: a comparative study. Mater Res Express 6(2):025508

Foroutan R, Mohammadi R, Adeleye AS, Farjadfard S, Esvandi Z, Arfaeinia H, Sorial GA, Ramavandi B, Sahebi S (2019a) Efficient arsenic(V) removal from contaminated water using natural clay and clay composite adsorbents. Environ Sci Pollut Res Int 26(29): 29748–29762

Foroutan R, Mohammadi R, Farjadfard S, Esmaeili H, Ramavandi B, Sorial GA (2019b) Eggshell nano-particle potential for methyl violet and mercury ion removal: surface study and field application. Adv Powder Technol 30(10):2188–2199

Foroutan R, Mohammadi R, Farjadfard S, Esmaeili H, Saberi M, Sahebi S, Dobaradaran S, Ramavandi B (2019c) Characteristics and performance of Cd, Ni, and Pb bio-adsorption using Callinectes sapidus biomass: real wastewater treatment. Environ Sci Pollut Res Int 26(7):6336–6347

Foroutan R, Mohammadi R, Razeghi J, Ramavandi B (2019d) Performance of algal activated carbon/Fe$_3$O$_4$ magnetic composite for cationic dyes removal from aqueous solutions. Algal Res 40: 101509

Foroutan R, Mohammadi R, Sohrabi N, Sahebi S, Farjadfard S, Esvandi Z, Ramavandi B (2020) Calcined alluvium of agricultural streams as a recyclable and cleaning tool for cationic dye removal from aqueous media. Environ Technol Innov 17:100530

Fu H, Yang Y, Zhu R, Liu J, Usman M, Chen Q, He H (2018) Superior adsorption of phosphate by ferrihydrite-coated and lanthanum-decorated magnetite. J Colloid Interface Sci 530:704–713

Guo Y, Xing X, Shang Y, Gao B, Zhang L, Yue Q, Qian L, Wang Z (2019) Multiple bimetallic (Al-La or Fe-La) hydroxides embedded in cellulose/graphene hybrids for uptake of fluoride with phosphate surroundings. J Hazard Mater 241:241–248

Halajnia A, Oustan S, Najafi N, Khataee AR, Lakzian A (2013) Adsorption–desorption characteristics of nitrate, phosphate and sulfate on Mg–Al layered double hydroxide. Appl Clay Sci 80-81: 305–312

Hatami H, Fotovat A, Halajnia A (2018) Comparison of adsorption and desorption of phosphate on synthesized Zn-Al LDH by two methods in a simulated soil solution. Appl Clay Sci 152:333–341

Hu F, Wang M, Peng X, Qiu F, Zhang T, Dai H, Liu Z, Cao Z (2018) High-efficient adsorption of phosphates from water by hierarchical CuAl/biomass carbon fiber layered double hydroxide. Colloids Surf A Physicochem Eng Asp 555:314–323

Iftekhar S, Kucuk ME, Srivastava V, Repo E, Sillanpaa M (2018) Application of zinc-aluminium layered double hydroxides for adsorptive removal of phosphate and sulfate: equilibrium, kinetic and thermodynamic. Chemosphere 209:470–479

Jang J, Lee DS (2019) Effective phosphorus removal using chitosan/Ca-organically modified montmorillonite beads in batch and fixed-bed column studies. J Hazard Mater 375:9–18

Jia Y, Wang H, Zhao X, Liu X, Wang Y, Fan Q, Zhou J (2016) Kinetics, isotherms and multiple mechanisms of the removal for phosphate by Cl-hydrocalumite. Appl Clay Sci 129:116–121

Kong L, Tian Y, Wang Y, Li N, Liu Y, Pang Z, Huang X, Li M, Zhang J, Zuo W (2019) Periclase-induced generation of flowerlike clay-based layered double hydroxides: a highly efficient phosphate scavenger and solid-phase fertilizer. Chem Eng J 359:902–913

Lai L, Xie Q, Chi L, Gu W, Wu D (2016) Adsorption of phosphate from water by easily separable Fe$_3$O$_4$@SiO$_2$ core/shell magnetic nanoparticles functionalized with hydrous lanthanum oxide. J Colloid Interface Sci 465:76–82

Li R, Wang JJ, Zhou B, Awasthi MK, Ali A, Zhang Z, Gaston LA, Lahori AH, Mahar A (2016a) Enhancing phosphate adsorption by Mg/Al layered double hydroxide functionalized biochar with different Mg/Al ratios. Sci Total Environ 559:121–129

Li R, Wang JJ, Zhou B, Awasthi MK, Ali A, Zhang Z, Lahori AH, Mahar A (2016b) Recovery of phosphate from aqueous solution by magnesium oxide decorated magnetic biochar and its potential as phosphate-based fertilizer substitute. Bioresour Technol 215:209–214

Li R, Wang JJ, Zhang Z, Awasthi MK, Du D, Dang P, Huang Q, Zhang Y, Wang L (2018) Recovery of phosphate and dissolved organic matter from aqueous solution using a novel CaO-MgO hybrid carbon composite and its feasibility in phosphorus recycling. Sci Total Environ 642:526–536

Li JR, Wang FK, Xiao H, Xu L, Fu ML (2019) Layered chalcogenide modified by lanthanum, calcium and magnesium for the removal of phosphate from water. Colloids Surf A Physicochem Eng Asp 560: 306–314

Lin J, He S, Wang X, Zhang H, Zhan Y (2019a) Removal of phosphate from aqueous solution by a novel Mg(OH)$_2$/ZrO$_2$ composite: adsorption behavior and mechanism. Colloids Surf A Physicochem Eng Asp 561:301–314

Lin J, Wang X, Zhan Y (2019b) Effect of precipitation pH and coexisting magnesium ion on phosphate adsorption onto hydrous zirconium oxide. J Environ Sci 76:167–187

Martin E, Lalley J, Wang W, Nadagouda MN, Sahle-Demessie E, Chae SR (2018) Phosphate recovery from water using cellulose enhanced magnesium carbonate pellets: kinetics, isotherms, and desorption. Chem Eng J 352:612–624

Mortazavi SB, Ramavandi B, Moussavi G (2011) Chemical reduction kinetics of nitrate in aqueous solution by Mg/Cu bimetallic particles. Environ Technol 32(3–4):251–260

Najib N, Christodoulatos C (2019) Removal of arsenic using functionalized cellulose nanofibrils from aqueous solutions. J Hazard Mater 367:256–266

Novillo C, Guaya D, Allen-Perkins AA, Armijos C, Cortina JL, Cota I (2014) Evaluation of phosphate removal capacity of Mg/Al layered double hydroxides from aqueous solutions. Fuel 138:72–79

Ogata F, Imai D, Toda M, Otani M, Kawasaki N (2016) Properties of a novel adsorbent produced by calcination of nickel hydroxide and its capability for phosphate ion adsorption. J Ind Eng Chem 34:172–179

Okoli CP, Ofomaja AE (2019) Development of sustainable magnetic polyurethane polymer nanocomposite for abatement of tetracycline antibiotics aqueous pollution: response surface methodology and adsorption dynamics. J Clean Prod 217:42–55

Okoli CP, Adewuyi GO, Zhang Q, Diagboya PN, Guo Q (2014) Mechanism of dialkyl phthalates removal from aqueous solution using gamma-cyclodextrin and starch based polyurethane polymer adsorbents. Carbohydr Polym 114:440–449

Okoli CP, Adewuyi GO, Zhang Q, Zhu G, Wang C, Guo Q (2015) Aqueous scavenging of polycyclic aromatic hydrocarbons using epichlorohydrin, 1,6-hexamethylene diisocyanate and 4,4-methylene diphenyl diisocyanate modified starch: pollution remediation approach. Arab J Chem 22:787–794

Ooi K, Sonoda A, Makita Y, Torimura M (2017) Comparative study on phosphate adsorption by inorganic and organic adsorbents from a diluted solution. J Environ Chem Eng 5(4):3181–3189

Ramavandi B, Mortazavi SB, Moussavi G, Khoshgard A, Jahangiri M (2011) Experimental investigation of the chemical reduction of nitrate ion in aqueous solution by Mg/Cu bimetallic particles. React Kinet Mech Catal 102(2):313–329

Ramavandi B, Jafarzadeh M, Sahebi S (2013) Removal of phenol from hyper-saline wastewater using Cu/Mg/Al–chitosan–H_2O_2 in a fluidized catalytic bed reactor. React Kinet Mech Catal 111(2):605–620

Rashid M, Price NT, Gracia Pinilla MA, O'Shea KE (2017) Effective removal of phosphate from aqueous solution using humic acid coated magnetite nanoparticles. Water Res 123:353–360

Saberzadeh SF, Esmaeili H, Ramavandi B (2016) Modification of Sargassum angustifolium by molybdate during a facile cultivation for high-rate phosphate removal from wastewater: structural characterization and adsorptive behavior. Biotech 6(2):251

Sadeghalvad B, Azadmehr A, Hezarkhani A (2017) Sulfate decontamination from groundwater by metal layered double hydroxides functionalized high phosphorus iron ore waste as a new green adsorbent: experimental and modeling. Ecol Eng 106:219–230

Seftel EM, Ciocarlan RG, Michielsen B, Meynen V, Mullens S, Cool P (2018) Insights into phosphate adsorption behavior on structurally modified ZnAl layered double hydroxides. Appl Clay Sci 165:234–246

Shafiee M, Foroutan R, Fouladi K, Ahmadlouydarab M, Ramavandi B, Sahebi S (2019) Application of oak powder/Fe3O4 magnetic composite in toxic metals removal from aqueous solutions. Adv Powder Technol 30(3):544–554

Shams M, Nabipour I, Dobaradaran S, Ramavandi B, Qasemi M, Afsharnia M (2013) An environmental friendly and cheap adsorbent (municipal solid waste compost ash) with high efficiency in removal of phosphorus from aqueous solution. Fresenius Environ Bull 22:722–726

Vikrant K, Kim KH, Ok YS, Tsang DCW, Tsang YF, Giri BS, Singh RS (2018) Engineered/designer biochar for the removal of phosphate in water and wastewater. Sci Total Environ 616-617:1242–1260

Wan S, Wang S, Li Y, Gao B (2017) Functionalizing biochar with Mg–Al and Mg–Fe layered double hydroxides for removal of phosphate from aqueous solutions. J Ind Eng Chem 47:246–253

Wang D, Hu W, Chen N, Yu Y, Tian C, Feng C (2016a) Removal of phosphorus from aqueous solutions by granular mesoporous ceramic adsorbent based on Hangjin clay. Desalin Water Treat 57(47):22400–22412

Wang Z, Xing M, Fang W, Wu D (2016b) One-step synthesis of magnetite core/zirconia shell nanocomposite for high efficiency removal of phosphate from water. Appl Surf Sci 366:67–77

Xi Y, Huang M, Luo X (2019) Enhanced phosphate adsorption performance by innovative anion imprinted polymers with dual interaction. Appl Surf Sci 467-468:135–142

Yan LG, Yang K, Shan RR, Yan T, Wei J, Yu SJ, Yu HQ, Du B (2015) Kinetic, isotherm and thermodynamic investigations of phosphate adsorption onto core-shell Fe_3O_4@LDHs composites with easy magnetic separation assistance. J Colloid Interface Sci 448:508–516

Yang K, Yan LG, Yang YM, Yu SJ, Shan RR, Yu HQ, Zhu BC, Du B (2014) Adsorptive removal of phosphate by Mg–Al and Zn–Al layered double hydroxides: kinetics, isotherms and mechanisms. Sep Purif Technol 124:36–42

Yang F, Zhang S, Sun Y, Tsang DCW, Cheng K, Ok YS (2019) Assembling biochar with various layered double hydroxides for enhancement of phosphorus recovery. J Hazard Mater 365:665–673

Zhan T, Zhang Y, Yang Q, Deng H, Xu J, Hou W (2016) Ultrathin layered double hydroxide nanosheets prepared from a water-in-ionic liquid surfactant-free microemulsion for phosphate removal from aquatic systems. Chem Eng J 302:459–465

Zhang M, Gao B, Yao Y, Inyang M (2013) Phosphate removal ability of biochar/MgAl-LDH ultra-fine composites prepared by liquid-phase deposition. Chemosphere 92(8):1042–1057

Zhang B, Chen N, Feng C, Zhang Z (2018) Adsorption for phosphate by crosslinked/non-crosslinked-chitosan-Fe(III) complex sorbents: characteristic and mechanism. Chem Eng J 353:361–372

Zhong L, Liang CS, Cui JY, Cai YB, Xu AS (2015) Magnetically recoverable mesoporous melamine–formaldehyde nanoparticles as an efficient adsorbent for hexavalent chromium removal. Electron Suppl Mater 421:441–452